

MDPI

Article

Research on Modified Thermal Barrier Coatings Against CMAS Corrosion Driven by Mechanism-Data Hybrid Model

Dongdong Ye ¹, Feixiang Wu ¹, Zhou Xu ^{2,*}, Yiwen Wu ³, Changdong Yin ², Huanjie Fang ^{4,*} and Houli Liu ^{1,*}

- School of Artificial Intelligence, Anhui Polytechnic University, Wuhu 241000, China; ddyecust@ahpu.edu.cn (D.Y.); 2220140102@stu.ahpu.edu.cn (F.W.)
- School of Electrical and Automation, Wuhu Institute of Technology, Wuhu 241006, China; 101044@whit.edu.cn
- Institute of Intelligent Manufacturing, Wuhu Institute of Technology, Wuhu 241006, China; 101138@whit.edu.cn
- ⁴ Key Laboratory of Advanced Marine Materials, Ningbo Institute of Materials Technology and Engineering of the Chinese Academy of Sciences, Ningbo 315201, China
- * Correspondence: 101043@whit.edu.cn (Z.X.); fanghuanjie@nimte.ac.cn (H.F.); hlliu@ahpu.edu.cn (H.L.)

Abstract: With the development of high-efficiency gas turbine engines and increasing inlet temperatures, the performance of thermal barrier coatings (TBCs) for hot-section components has been more severely challenged. The doping of multi-element rare earth elements significantly improves the thermodynamic properties and chemical compatibility of thermal barrier coatings so that the application performance of coatings in high-temperature environments is enhanced considerably. In this work, the doped coatings prepared by REYSZ (RE = La, Sm, Nd) were investigated and characterized in terms of crystal structure, elastic properties, and thermal-mechanical properties based on the first-principles approach, combined with various empirical and semi-empirical formulations, and a predictive model for resistance to CMAS corrosion based on machine learning approaches. The results showed that the tetragonal phase REYSZ material was mechanically stable, had a large strain damage tolerance, and was not easy to fracture under applied loads and thermal shocks. In terms of CMAS corrosion resistance, the NdYSZ interfacial model had a lower surface energy (3.130 J/m²) and Griffith fracture energy (6.934 J/m²) compared with the conventional YSZ model, and Nd₂O₃ had the potential to improve the CMAS corrosion resistance of zirconia-based material for thermal barrier coatings. By evaluating the machine learning prediction models, the regression coefficients of the two algorithms were 0.9627 and 0.9740, and both these two prediction models showed high prediction accuracy and strong robustness. Ultimately, this work presented a novel mechanism-data hybrid method, which would facilitate the efficient development of TBC new materials for anti-CMAS corrosion.

Keywords: thermal barrier coatings; rare earth doping; first principles; machine learning



Citation: Ye, D.; Wu, F.; Xu, Z.; Wu, Y.; Yin, C.; Fang, H.; Liu, H. Research on Modified Thermal Barrier Coatings Against CMAS Corrosion Driven by Mechanism–Data Hybrid Model. *Coatings* 2024, 14, 1513. https://doi.org/10.3390/coatings14121513

Academic Editor: Ben Beake

Received: 31 October 2024 Revised: 25 November 2024 Accepted: 27 November 2024 Published: 30 November 2024



Copyright: © 2024 by the authors. Licensee MDPI, Basel, Switzerland. This article is an open access article distributed under the terms and conditions of the Creative Commons Attribution (CC BY) license (https://creativecommons.org/licenses/by/4.0/).

1. Introduction

The high-performance aero-engine is a collection of high-precision technology, and its manufacturing capacity is an important indicator of a country's scientific and technological industrial level. To improve the efficiency and performance of the engine, the inlet temperature of the turbine engine will exceed 1500 °C, which will cause the hot-end components of the engine to undergo more severe service tests. Therefore, thermal barrier coatings (TBCs) technology and cooling gas film technology were introduced to protect superalloys. Thermal barrier coatings are a widely used high-temperature protection technology for hot-end components of gas turbines. Its principle is to use ceramics with low thermal conductivity, high-temperature resistance, and corrosion resistance to combine with the metal matrix in the form of coatings and to effectively reduce the surface temperature of the hot-end components so that the superalloys could be used safely for a long time in an environment far higher than its melting points [1–3]. For decades, 6–8 wt.% Yttria Partially

Coatings **2024**, 14, 1513 2 of 21

Stabilized Zirconia (YSZ) has been recognized as a successful thermal barrier coatings material in the industry, which combines the requirements of low thermal conductivity, high fracture toughness, and a relatively high thermal expansion coefficient in an excellent way [4,5]. However, with the further increase in operating temperature, TBC systems face challenges. In particular, Calcium–Magnesium–Alumino–Silicates (CMAS) particles inhaled by the engine are considered to be an unavoidable problem that will lead to severe degradation and spalling of the ceramic layer [6–8]. The specific corrosion mode is as follows: The molten CMAS attacks the TBCs as a moving front rapidly penetrates into the pores and cracks of the TBCs and then dissolves the zirconia. At the same time, it precipitates, expands in volume, and eventually reaches the metal substrate and reacts with the bonding layer and the substrate. The infiltration process can lead to damage to the strain tolerance of TBCs, thus making them highly susceptible to mechanical failure during thermal cycling [9–12].

The problem of coating spalling due to molten silicate corrosion will further deteriorate as the operating temperature increases. The complex microstructure and material composition of the thermal barrier coatings aggravate the complexity and multiplicity of coating failure forms. Aiming at the current situation that the traditional 6~8 wt.% yttrium oxide partially stabilized zirconia (6-8YSZ) thermal barrier coatings are susceptible to CMAS erosion at high temperatures, researchers have explored a lot of CMAS corrosion protection technology for thermal barrier coatings, but there are still problems such as a poor long-time protection effect and short service life of the coating. A common solution today is to prepare a protective coating on the surface of a conventional coating. These materials have excellent performance in terms of CMAS corrosion resistance; nevertheless, their poor thermomechanical properties lead to frequent spalling failure of the coatings during cold-heat cycling, which greatly limits the usefulness of these materials. For example, the work of Guo et al. [13] demonstrated that newly developed LnPO₄ (Ln = La, Gd) TBCs could effectively inhibit the penetration of molten CMAS. However, the thermal compatibility between the coatings and CMAS needs to be further improved. In addition to depositing a kind of protective layer on the surface of thermal barrier coatings, related studies have shown that rare earth (RE) element doping is a commonly used means of material modification, which could significantly improve the service performance of thermal barrier coatings [14]. Doping of large-size rare earth elements (La³⁺, Nd³⁺, and Gd³⁺) could effectively improve the high-temperature sintering resistance of the coating while doping of small-size rare earth elements could improve the phase stability [15]; Song et al. [16], in order to improve the thermal corrosion resistance of YSZ coatings against Na₂SO₄ + V₂O₅, doped them with trace amounts of the rare earth elements Yb, Gd, and prepared 5.6Yb₂O₃. -5.2Gd₂O₃-9.5Y₂O₃-ZrO₂ (YGYZ) coating was prepared. The results showed that after thermal corrosion at 1374.15 K for 20 h, the degradation of m-ZrO₂ in the YGYZ coatings is only about 40% of that of the YSZ coating, and the YGYSZ coating has high tetragonal properties. To improve the thermal conductivity of the La₂Zr₂O₇ coatings, Gul [17] et al. doped the rare earth element Ce in this coating, and the doping of Ce element was found to have a significant effect on the thermal conductivity of La₂Zr₂O₇ coatings.

Therefore, based on YSZ material or zirconia material, designing new material for thermal barrier coatings through rare earth doping modification to meet the functions of CMAS corrosion resistance and thermal insulation is currently a more practical approach. The mechanism utilizes a chemical reaction between a highly chemically active thermal barrier coating material and the CMAS melt. Formation of high melting point corrosion products, so as to achieve the sealing of open pores on the surface of the coating, achieves the purpose of slowing down the penetration of molten CMAS. Due to the lack of necessary theoretical guidance, the development of new CMAS corrosion-resistant thermal barrier coating materials is mainly through the Edison experimental method; i.e., a material is selected and experimentally proven until successful. Experimental methods provide a more intuitive assessment of material performance, but, at the same time, greatly increase the time and cost wasted in conventional trial-and-error processes. With so many known

Coatings **2024**, 14, 1513 3 of 21

crystal structures in mineralogy and crystal chemistry, each of which can be composed of several different elements, there is a needle in a haystack when it comes to experimentally sifting through tens of thousands of materials to find a suitable CMAS corrosion-resistant thermal barrier coating material.

In summary, this paper takes zirconia material as a prototype and utilizes first-principle calculations to investigate the effects of different rare earth element doping on the thermodynamic properties and CMAS corrosion resistance of the material by modeling the doping and then comparing it with conventional thermal barrier coating materials in terms of CMAS corrosion resistance, the coefficient of thermal expansion, thermal conductivity, fracture toughness, and hardness in a comprehensive manner. Finally, a prediction model for CMAS corrosion resistance is established through simulation data combined with machine learning methods to further verify the accuracy and robustness of the secondary validation model driven by both mechanisms and data. The results show that the high-throughput screening method for novel thermal barrier coating materials developed based on first-principle computational methods can effectively predict the corrosion resistance and thermophysical properties of materials against CMAS, which is of guiding significance for the development and design of novel thermal barrier coating materials. This paper addresses the lack of theoretical guidance for the development of materials for CMAS corrosion-resistant thermal barrier coatings, attempting to go deeper into the atomic perspective from first-principles calculations and developing a simple and efficient highthroughput screening method for thermal barrier coating materials. Effective prediction of CMAS corrosion resistance and other thermal and mechanical properties of thermal barrier coating materials to guide experiments is provided.

2. Materials and Methods

2.1. First Principles

Using first-principles calculations based on density functional theory (DFT), four stable supercell models with tetragonal phase structure were developed and analyzed based on tetragonal phase zirconia cell parameters reported in the literature [18,19], namely, YSZ $(Y_4Zr_{12}O_{30})$, LaYSZ $(La_2Y_2Zr_{12}O_{30})$, SmYSZ $(Sm_2Y_2Zr_{12}O_{30})$, and NdYSZ $(Nd_2Y_2Zr_{12}O_{30})$, collectively referred to as (REYSZ), and are shown in Figure 1a-d. In order to establish a correct doping model, it was first necessary to clarify the relationship between the substitution positions of rare earth elements and oxygen vacancies. When four orthotrivalent rare earth atoms (RE^{3+}) replaced ortho-tetravalent zirconium atoms (Zr^{4+}), the system assumed electronegativity. Therefore, two oxygen atoms in the cell must be removed in order to form oxygen vacancies. As shown in Figure 1e, a tetragonal phase zirconia cell could be seen with eight oxygen atoms surrounding the central zirconium atom and the first and second nearest neighbor sites, respectively. When the central zirconium atom was replaced by a rare earth element, the oxygen vacancies were more inclined to occupy the second nearest-neighbor site of the larger dopant and the first nearest-neighbor site of the smaller dopant, and this crossover occurred approximately at the Sc element. Through these steps, the rare earth element doped zirconia cell model was successfully constructed.

All calculations in this work were performed using ab initio quantum mechanical and quantum chemical procedures based on density functional theory. The crystal structure and elastic properties of the doped model were investigated using the theory of plane-wave pseudopotential total energy calculations. To obtain a local steady state, the model was fully relaxed before the performance and energy calculations, and the convergence criterion was set uniformly as the Perdew–Burke–Ernzerhof (PBE) potential function based on the generalized gradient approximation (GGA) that was used to deal with the correlation energy of the electron exchange in the inverse easy space, with the truncation energy chosen to be 489.8 eV, and the root mean square forces and stresses were set to be 0.03 eV/Å and 0.01 GPa, the displacement was chosen to be 0.002 Å, and the convergence criterion for both the self-consistent field and the energy tolerance was set to 5.0×10^{-4} eV/atom, using the BFGS algorithm with the OTFG paradigm-conserving pseudopotential. The

Coatings **2024**, 14, 1513 4 of 21

elastic constants were determined by first-principles calculations, and the internal degrees of freedom were optimized by applying a prescribed set of finite-valued homogeneous deformations and calculating the resulting stresses, and then the elastic stiffness constants and associated equations were used to obtain the thermomechanical properties such as elastic modulus, Poisson's ratio, Vickers' hardness, and the mean speed of sound. When constructing the interface model, the vacuum layer thickness was taken as 15 Å. To balance the computational accuracy and computational volume, the number of k-point lattices in the Brillouin zone was set to $4 \times 4 \times 3$ for the system of smaller basic cells, while the number of k-point lattices was taken as $2 \times 2 \times 1$ for the system of larger atomic number.

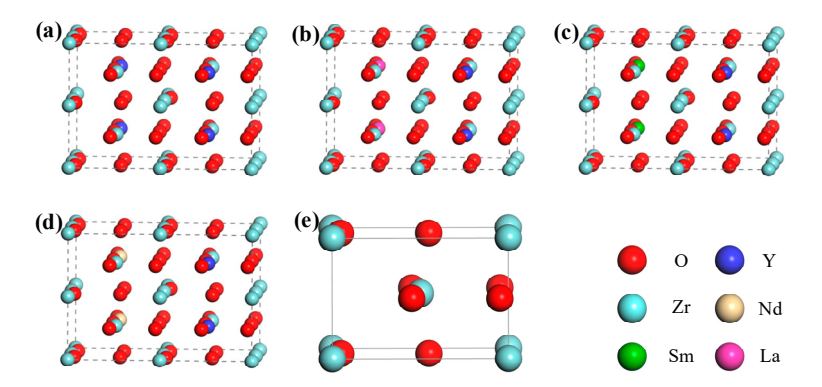


Figure 1. Theoretical calculation models of rare earth element doped YSZ: (a) YSZ supercell; (b) LaYSZ supercell; (c) SmYSZ supercell; (d) NdYSZ supercell; and (e) tetragonal phase ZrO₂ base cell.

2.2. Corrosion Resistance to CMAS

The material system was a key factor in determining the CMAS corrosion resistance of thermal barrier coatings. Therefore, the search for new material for thermal barrier coatings that could inhibit and mitigate CMAS corrosion has been a hot research topic in recent years. The wetting characteristics of materials played a crucial role in improving the CMAS corrosion resistance of thermal barrier coatings. Excellent wetting resistance was beneficial to the separation of liquid CMAS during the high-speed operation of turbine blades. In this work, the wetting properties of the materials were predicted using first-principle calculations, and the wetting resistance was evaluated by two parameters, namely, Griffith fracture energy and surface energy. Through the surface energy calculation, the stable surface structure with the lowest energy was selected to be constructed with the amorphous CMAS cell to obtain the interface model, as shown in Figure 2.

Due to the limitation of the cellular model, a simplified model of the CMAS amorphous model was obtained as Ca₈Mg₁A₁₄Si₁₀ based on the composition and content of the homemade CMAS powder in the laboratory. At the engine operating temperature, CMAS melted and solidified into a glassy phase at temperatures below the melting point. In order to investigate its properties, the construction of the CMAS amorphous model was first carried out using the amorphous cell module of the software. Oxide mixing was performed using the four oxide base elements, which were then fused into the lattice to obtain an amorphous CMAS model. The obtained amorphous model was geometrically optimized and subjected to molecular dynamics simulations. The CMAS amorphous model was first optimized at a 1550 °C environment to ensure its local stability in the melting state. Subsequently, the relaxation was performed again at the experimental temperature of 1300 °C to obtain the final CMAS amorphous model. Before constructing the interfacial model, the surface models of individual rare earth-doped zirconia supercells needed to be obtained. By cutting the supercell model along the {1 1 1} Miller exponential crystal plane, surface models with different atomic arrangements could be obtained. For a given model, the surface energy was calculated using the following equation [20]:

$$E_{surface} = \frac{1}{2A}(E_{slab} - NE_{bulk}) \tag{1}$$

Coatings **2024**, 14, 1513 5 of 21

where $E_{surface}$ was the model surface energy, E_{slab} denoted the total energy of the protocells, A represented the model cross-sectional area, and N was the number of protocells; in this simulation, A and N were taken as 50.9028675 $Å^2$ and 2, respectively.

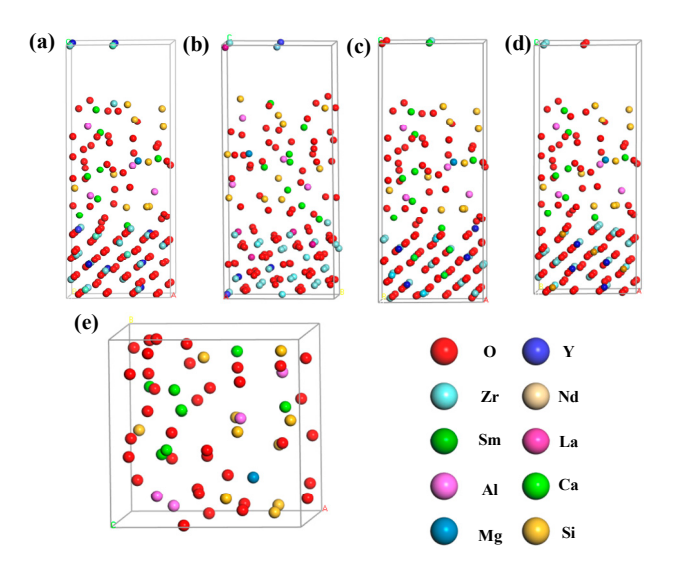


Figure 2. Theoretical calculation models of CMAS corrosion: (a) CMAS/YSZ interface model; (b) CMAS/LaYSZ interface model; (c) CMAS/SmYSZ interface model; (d) CMAS/NdYSZ interface model; and (e) amorphous CMAS crystal cell.

The Griffith fracture energy represented the work required to separate an interfacial model into two separate free surface models along a perpendicular interfacial direction and could be used to assess the bond strength of the interface. By definition, the Griffith fracture energy was calculated as follows [21]:

$$W = \frac{E_{total} - E_{CMAS} - E_{REYSZ}}{A} \tag{2}$$

where E_{total} was the total interface model energy, E_{CMAS} was the CMAS amorphous model energy, E_{REYSZ} was the rare earth-doped zirconia REYSZ model energy, and A was the cross-sectional area. Combined with the relationship between interfacial bond strength and wetting angle [22],

$$W_{sL} = \gamma_L (1 + \cos \theta) \tag{3}$$

where W_{sL} denoted the interfacial bond strength, γ_L was the liquid surface tension, and θ was the wetting angle. According to Equations (2) and (3), it was not difficult to derive the relationship between Griffith fracture energy, interfacial bond strength, and wetting angle: The larger the Griffith fracture energy was, the larger the interfacial bond strength was, the smaller the wetting angle was, and the worse the CMAS wetting resistance was.

2.3. Data-Driven Predictive Modeling

2.3.1. BP Neural Networks

BP neural network is a classic machine learning algorithm; the principle is to train the network through the backpropagation algorithm according to the difference between the actual output and the desired output to optimize the network's weights and bias, with the advantages of having simple structure, being easy to use, and being widely applicable [23,24]. The basic flow of the BP neural network was shown in Figure 3, and the algorithm covered the two main processes of forward propagation of the signal and backpropagation of the error. The former generally used the sigmoid transform function to construct a nonlinear mapping network between the input and output signals and transferred to the error backpropagation process by calculating the generalized error between the actual output and the desired output. This process apportioned the error to

Coatings **2024**, 14, 1513 6 of 21

all units in each layer and used the gradient descent method and other methods to find the optimal combination of node connection weights and thresholds in each layer so as to minimize the overall network mean square error. In general, researchers controlled the network generation by specifying the error precision or the maximum number of learning times, with an intention to accelerating the network convergence and avoiding the dilemma of local optimum.

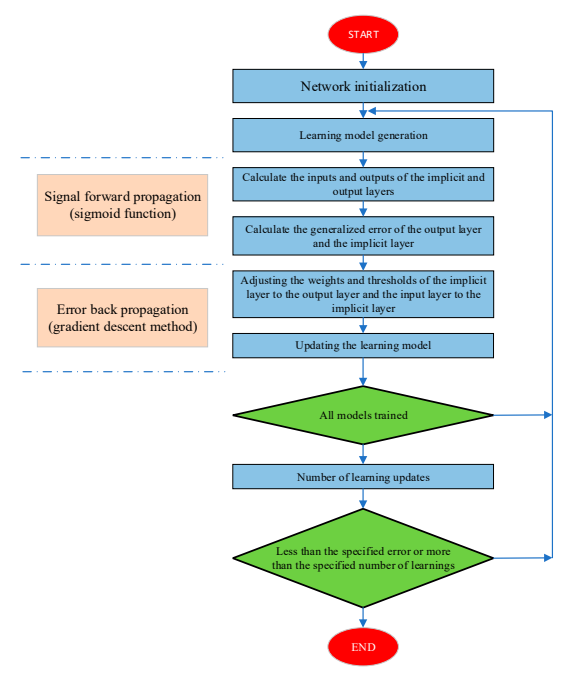


Figure 3. Basic flow chart of BP neural network.

2.3.2. Extreme Learning Machines

Extreme learning machine (ELM) was a new type of single hidden layer forward network with excellent performance proposed by Huang Guangbin [25] in 2006 based on generalized inverse matrix theory. Compared with traditional neural networks, the output weights of the network could be resolved by only one step of calculation, which greatly improved the generalization ability and learning speed of the network, have strong nonlinear fitting ability, and greatly reduced the amount of computation and search space. The structure of ELM was shown in Figure 4, which consisted of three parts: the input layer, the hidden layer, and the output layer. The input and hidden layers were connected by input weights W and hidden layer bias b. The hidden layer and output layer were connected by output weights β . For an ELM with the number of hidden layers L, assuming the training set $X_j = [x_1, x_2, \dots, x_N]T \in Rn$ and $T_j = [t_1, t_2, \dots, t_n]T \in Rm$, the computation process of the ELM could be expressed as follows [26]:

$$f_L(X) = \sum_{i=1}^{L} \beta_i g_i(X) = \sum_{i=1}^{L} \beta_i g(W_i \cdot X_j + b_i), j = 1, \dots, N$$
 (4)

where N was the number of samples in the training set; g was the activation function; Wi was the input weight, $W_i = [\omega_1, \omega_2, \dots, \omega_n]$; β_i was the output weight; b_i was the bias of the ith neuron in the hidden layer.

Coatings 2024, 14, 1513 7 of 21

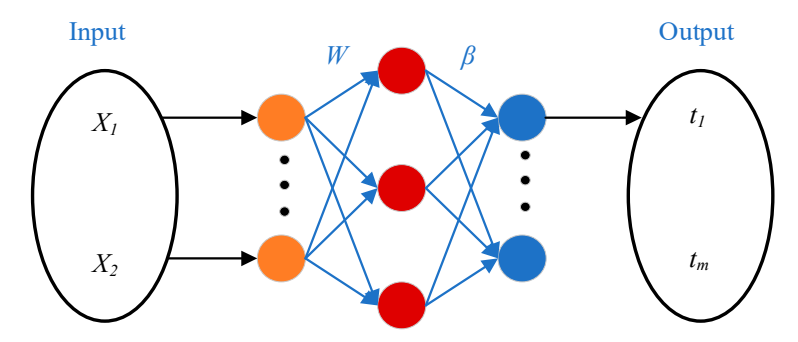


Figure 4. Typical structure of ELM.

2.3.3. Cross-Validation

Cross-validation was an important statistical technique for evaluating the performance of machine learning models and selecting the best parameters, and K-fold cross-validation was one of the most widely used methods [27]. The dataset was randomly divided into K subsets, where K-1 subsets were used to train the model, while the remaining one was used to evaluate the model performance. This process would be repeated K times, each time using a different subset as the validation set, and finally, the results of the K evaluations would be averaged to obtain the final performance metric.

As shown in Figure 5, the training set was partitioned into 5 subsets, each of which would be rotated as part of the validation set, while the remaining 4 subsets form the training set. Then, in each cross-validation iteration, a machine learning algorithm was used for model training using the 4 subsets as the training set. The performance of the model on this validation set was then evaluated using one of the remaining subsets as the validation set. By trying different parameter combinations and evaluating the model performance with cross-validation results, the most suitable parameter combinations for the dataset could be found to improve the predictive and generalization capabilities of the model. In this way, the performance of the model could be assessed more comprehensively, and the optimal parameter configuration could be selected efficiently. Cross-validation was a powerful tool to effectively improve the accuracy and stability of machine learning models.

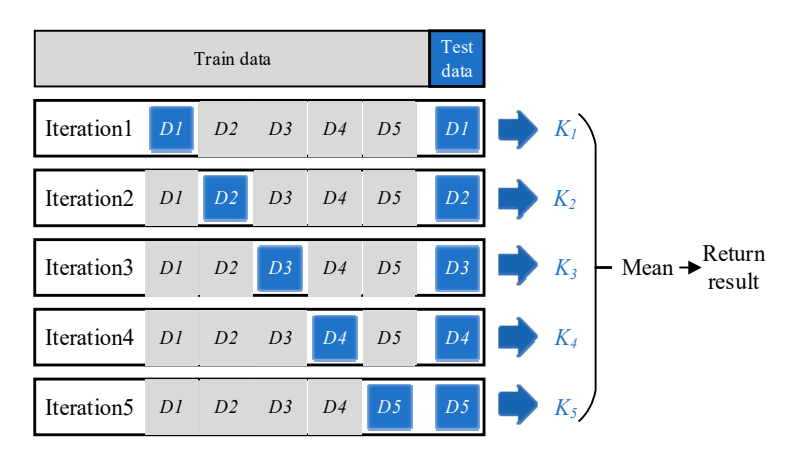


Figure 5. Schematic diagram of cross-validation.

Performance evaluation plays a crucial role in machine learning model training. Each cross-validation iteration was a test of the model's true capability, recording the model's performance on the validation set, such as accuracy, precision, and other metrics. The average of these metrics was the basis for the final assessment of the model's performance, which could provide an objective evaluation result. The cross-validation method could not only reflect the generalization ability of the model more objectively but also effectively avoid overfitting or underfitting problems and improve the stability of the model. In this work, the 5-fold cross-validation method was adopted, and the results of each round of

Coatings **2024**, 14, 1513 8 of 21

iteration were recorded and analyzed in detail to verify the reliability and accuracy of the established prediction model.

3. Results

3.1. Lattice Structure and Stability Analysis

Studies in structural properties played an important role in the microscopic understanding of the physical properties of doping models. As shown in Figure 1, a $2 \times 2 \times 2$ supercell model with 46 atoms was used for the calculations, and the tetragonal phase zirconia base cell structure had two lattice constants, a and c. To ensure the reliability of the calculations, the structural information obtained from full geometrical optimization of the crystal structure was summarized in Table 1.

Table 1. Lattice constant (Å), volume (Å³), density (g/cm³), formation energy (eV/atom), and ground state energy E_{bulk}/eV after doping model optimization.

| Crystal | а | SNN | V | ρ | E_f | E_{bulk} |
|---------|-------|--------|---------|-------|---------|---------------|
| YSZ | 7.380 | 10.716 | 591.458 | 5.419 | -8.587 | 33,078.98941 |
| LaYSZ | 7.493 | 10.624 | 581.830 | 5.794 | -13.122 | -32,890.35333 |
| NdYSZ | 7.315 | 0.55 | 569.991 | 5.946 | -7.086 | -34,333.20421 |
| SmYSZ | 7.309 | 0.52 | 567.824 | 6.004 | -5.728 | -35,754.78252 |

As shown in Table 1, the equilibrium lattice constants obtained after optimization of several doping models were close to each other, and the difference between the lattice constants before and after optimization was less than 5%, which proved the stability of the model structure. With the increase in the atomic number of lanthanide rare earth elements, the lattice constant decreased, the cell volume shrank, the density of the material increased, and the base energy showed a trend of gradual increase. The enthalpy of formation was the energy released (absorbed) by the system during the formation of compounds from monomers. The enthalpy of formation was usually negative, and the larger the negative value of the enthalpy of formation, the more stable the structure of the compound was. To determine the thermodynamic stability of the REYSZ doping model, this work calculated the enthalpy of the formation of the material by the following equation [28]:

$$\Delta H = [E_{total} - xE_{bulk}(RE) - yE_{bulk}(Zr) - zE_{bulk}(O)]/(x+y+z)$$
(5)

where E_{total} was the total energy of the REYSZ doping system, and E_{bulk} was the single atom energy of each element in the equilibrium crystal structure system. As shown in Table 1, the enthalpies of the formation of REYSZ were all negative, indicating that the formation of the compound system was an exothermic process; i.e., the material was thermodynamically stable in the ground state.

The density of states (DOS) indicated the number of electrons allowed per unit energy range, i.e., the distribution of electrons in a certain energy range, reflecting the distribution of electrons in individual orbitals and interatomic bonding properties. To further understand the inter-orbital interactions between the model atoms under the effect of rare earth elements, the total DOS and partial density of states (PDOS) of the four doping systems were obtained using data processing. The calculation results were shown in Figure 6, where the dashed part represents the Fermi energy level, and the density of states curves of the REYSZ phases were not significantly different, indicating that no obvious change in the energy level structure was found, and none of the electronic density of states were zero near the Fermi energy level, indicating that all REYSZ phases exhibit metallic properties. As shown in Figure 6, the total density of states for the entire valence band energy was mainly provided by the p and d orbitals, at -5 to 0 eV by the p orbitals and at 0 to 10 eV by the d orbitals. In general, when studying crystalline materials, the relative stability of the material could be obtained by comparing the electronic density of states N(EF) at the Fermi energy level, and the smaller the value of N(EF), the more stable the structure was, and the

ordering of N(EF) was LaYSZ < YSZ < NdYSZ < SmYSZ, which was in agreement with the enthalpy of formation results. As shown in Figure 6, the N(EF) values of the two phases YSZ and LaYSZ were closer to each other, with the p-orbitals providing the energy near the Fermi energy level, and the doped rare earth elements Y and La contributing less to the Fermi energy level. The N(EF) values of the two phases NdYSZ and SmYSZ were closer to each other than the former two, and the stability of the structure decreased with the difference in the f orbitals, which were not present in the former two, providing the Fermi energy level. Near the Fermi energy level was a larger contribution to the total density of states by the rare earth elements Nd and Sm.

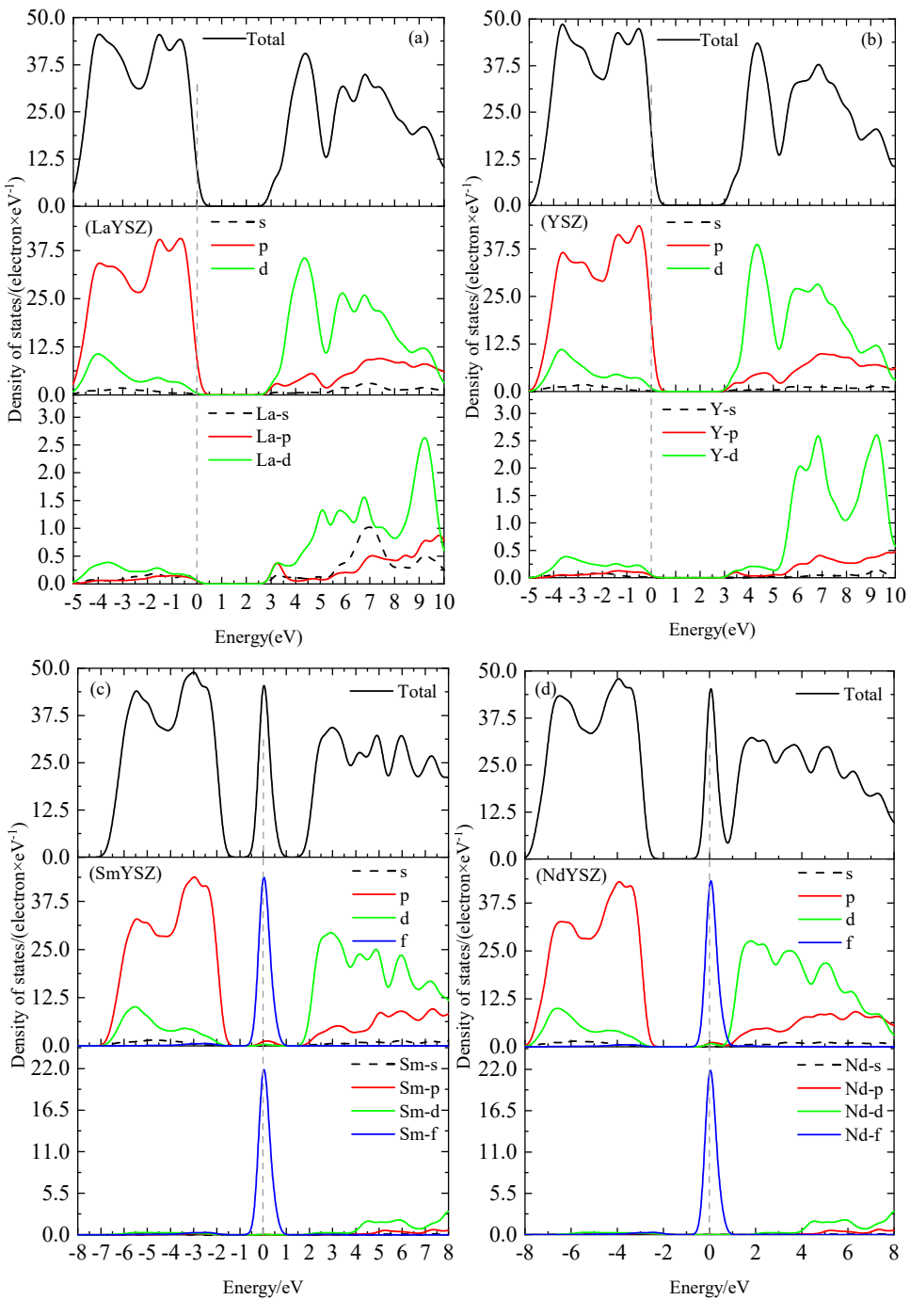


Figure 6. Total density of states (TDOS) and partitioned density of states (PDOS) maps for REYSZ. (a) LaYSZ state density map; (b) YSZ state density map; (c) SmYSZ state density map; (d) NdYSZ state density map.

Coatings 2024, 14, 1513 10 of 21

3.2. Thermo-Mechanical Property Analysis

3.2.1. Elastic Constants and Mechanical Stability Analysis

As shown in Table 2, it could be seen that the doping model fully satisfied the mechanical stability criterion, which proved that the tetragonal phase zirconia material had good mechanical stability. It was found by analyzing the elastic constants of the material:

| Table 2. Indepen | dent elastic | constants of | f the do | ping mod | el C _{ij} | (GPa) | |
|------------------|--------------|--------------|----------|----------|--------------------|-------|--|
|------------------|--------------|--------------|----------|----------|--------------------|-------|--|

| Crystal | C ₁₁ | C ₃₃ | C_{44} | C ₆₆ | C ₁₂ | C ₁₃ |
|---------|-----------------|-----------------|----------|-----------------|-----------------|-----------------|
| ZrO_2 | 383.29 | 351.34 | 52.33 | 168.89 | 233.04 | 75.91 |
| YSZ | 377.20 | 457.34 | 67.75 | 6.88 | 229.42 | 158.01 |
| LaYSZ | 406.08 | 453.43 | 73.63 | 19.40 | 243.33 | 196.71 |
| NdYSZ | 372.80 | 416.43 | 71.23 | 120.29 | 231.73 | 159.92 |
| SmYSZ | 361.71 | 386.20 | 69.23 | 81.63 | 224.70 | 169.71 |

In REYSZ compounds, $C_{11} < C_{33}$. C_{11} and C_{33} were parameters in the elastic constants reflecting the ability of the crystals to resist uniaxial linear compression, and $C_{11} < C_{33}$ indicated that the bulk modulus B of the material exhibited anisotropy. In the tetragonal phase crystal cell $C_{22} = C_{11}$, C_{33} was greater than the other elastic constants, indicating that REYSZ had the strongest unidirectional resistance to compression along the c-axis and was more easily compressed along the a-axis or b-axis. In general, C_{44} reflected the hardness of the material, and a higher C_{44} usually corresponded to higher hardness, which gradually decreased with an increasing atomic number of lanthanide rare earth elements in the REYSZ materials. In addition, C_{12} , C_{44} , and C_{66} were all moduli that described the ability of a material to resist shear deformation, and C_{44} and C_{66} were much smaller than C_{11} and C_{33} , suggesting that the material was more susceptible to shear deformation compared to unidirectional compression.

3.2.2. Analysis of Intrinsic Mechanical Parameters

The intrinsic mechanical parameters of REYSZ—bulk modulus *B*, shear modulus *G*, Young's modulus *E*, Poisson's ratio *v*, Pugh's ratio, and Cauchy's pressure—were predicted using *Vogit–Reuss–Hill* (VRH) approximation, and the results were shown in Table 3.

Table 3. Bulk elastic modulus (GPa), shear modulus (GPa), Young's modulus (GPa), Poisson's ratio, and Pugh's and Cauchy's pressures for doped models (GPa).

| Crystal | В | \boldsymbol{G} | E | v | G/B | C_{12} – C_{66} | C_{13} – C_{44} |
|---------|--------|------------------|--------|------|------|---------------------|---------------------|
| ZrO_2 | 205.83 | 91.10 | 238.17 | 0.31 | 0.44 | 64.15 | 23.58 |
| YSZ | 255.79 | 49.52 | 139.56 | 0.41 | 0.19 | 222.54 | 90.26 |
| LaYSZ | 282.12 | 62.93 | 175.73 | 0.40 | 0.22 | 223.93 | 123.08 |
| NdYSZ | 251.58 | 89.65 | 240.40 | 0.34 | 0.36 | 111.44 | 88.69 |
| SmYSZ | 248.50 | 78.91 | 214.06 | 0.36 | 0.32 | 143.07 | 100.48 |

The bulk modulus *B* was a parameter characterizing the relative shrinkage performance of the cell volume of a material under isotropic pressure, and the small difference in the bulk modulus of the REYSZ materials indicated that the materials were close to each other in their ability to resist volumetric deformation. Among them, LaYSZ had the largest bulk modulus, indicating that it was the most difficult to compress.

The shear modulus G represented the ability of a solid to resist tangential reversible deformation under shear stress, and a larger shear modulus usually corresponded to a larger C_{44} . As could be seen in Table 3, the shear moduli of REYSZ were in the order of NdYSZ > SmYSZ > LaYSZ > YSZ. Furthermore, the shear moduli of REYSZ were much smaller than the bulk modulus and Young's modulus, which also confirmed the above statement that REYSZ was more susceptible to shear stress.

Coatings 2024, 14, 1513 11 of 21

From the above relationships, it could be seen that both the coefficient of thermal expansion α and the thermal seismic performance R of the material show a roughly inverse relationship with the Young's modulus E. Therefore, a material with a lower Young's modulus had a higher coefficient of thermal expansion and better thermal shock resistance. The Young's modulus of REYSZ was ranked NdYSZ > SmYSZ > LaYSZ > YSZ, which was exactly the same as that of the shear modulus.

As shown in Table 3, it could be seen that the Push ratio G/B < 0.57, Poisson's ratio v > 0.26, and Cauchy's pressure was positive for the REYSZ material, which could be preliminarily determined as a ductile material.

3.2.3. Hardness, Fracture Toughness, and Damage Tolerance Analysis

As shown in Figure 7, the hardness of the REYSZ material was 10.069~13.398 GPa, and the highest hardness was 13.398 GPa for the traditional YSZ material, which was similar to the hardness of the rare earth element-doped material and thus meets the demand for the high hardness of the thermal barrier coating material. The mechanical properties of the material were shown in Table 4.

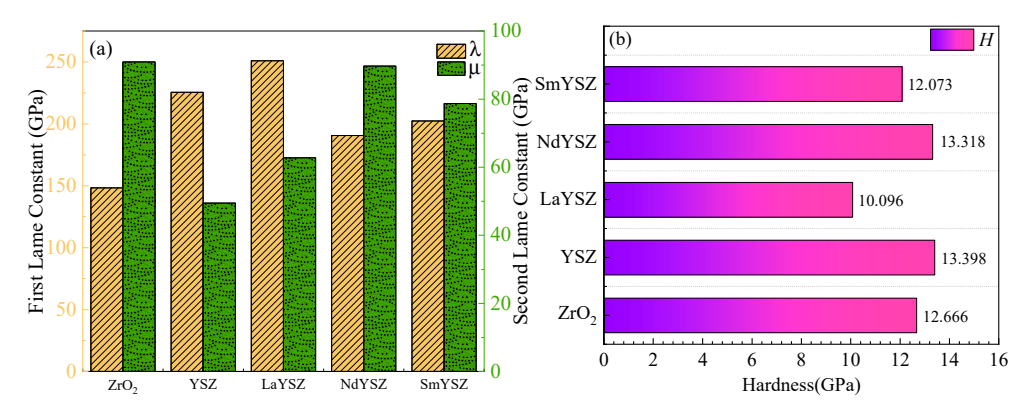


Figure 7. (a) Lame constant of REYSZ material and (b) hardness of REYSZ material.

Table 4. Lame constant (GPa), hardness (GPa), fracture toughness (MPa·m^{1/2}), critical energy release rate (J·m⁻²), and brittleness index (μ m^{-1/2}) of doped materials.

| Crystal | λ | μ | $H_{Mazhnik}$ | K_{IC} | $G_{\rm IC}$ | M |
|---------|---------|--------|---------------|----------|--------------|-------|
| ZrO_2 | 148.317 | 90.905 | 12.666 | 2.054 | 16.012 | 6.167 |
| YSZ | 225.45 | 49.489 | 13.398 | 1.722 | 17.674 | 7.780 |
| LaYSZ | 251.043 | 62.761 | 10.069 | 2.039 | 20.458 | 4.938 |
| NdYSZ | 190.616 | 89.701 | 13.318 | 2.283 | 19.289 | 5.834 |
| SmYSZ | 202.368 | 78.699 | 12.073 | 2.128 | 18.463 | 5.673 |

The fracture toughness value and critical energy release rate of the REYSZ materials were shown in Figure 8: The fracture toughness of the REYSZ materials was $1.722 \sim 2.283$ MPa-m^{1/2}. NdYSZ had the highest fracture toughness, and compared with the traditional YSZ materials doped with lanthanide rare earth elements, fracture toughness was improved, and with the increase in the atomic number of lanthanide rare earth, the material's critical release energy gradually decreased, which meant that the crack expansion of the material needed to absorb a larger amount of energy, which further proved that the REYSZ material had good fracture toughness. As shown in Figure 8, the brittleness indices of REYSZ materials were lower than that of conventional YSZ ($7.780 \ \mu m^{-1/2}$), which indicated that REYSZ materials had the ability to work for a long period of time in high-temperature environments. In summary, the hardness of REYSZ materials was 10.069-13.398 GPa, the fracture toughness was 1.722-2.283 MPa-m^{1/2}, the critical energy release rate was 17.674-20.458 J/m², and the brittleness index was 4.938-7.78 $\mu m^{-1/2}$. Among them, the best overall mechanical proper-

ties were those of NdYSZ (hardness 13.318 GPa and fracture toughness of 2.283 MPa-m^{1/2}), with good mechanical properties comparable to those of YSZ materials.

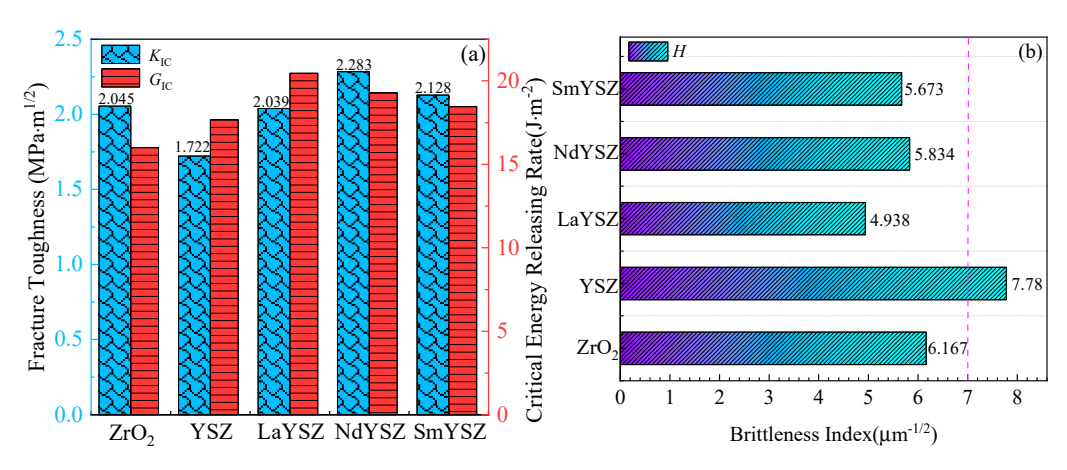


Figure 8. (a) Fracture toughness versus energy release correlation plot for REYSZ material and (b) brittleness index of REYSZ.

3.2.4. Melting Point and Débay Temperature Analysis

As shown in Table 5. For high-temperature structural materials, the melting point was closely related to the practicality and reliability of the material and was an important indicator of the material's high-temperature thermodynamic properties. In addition, the melting point of a material was the cornerstone of the study of its thermal expansion and bonding properties.

| Table 5. Melti | ng point (K) a | and Debye te | emperature (K | () of REYSZ materials. |
|----------------|----------------|--------------|---------------|------------------------|
| | | | | |

| Crystal | $T_{\mathbf{M1}}$ | $T_{	extbf{M2}}$ | Θ_{D} |
|---------|-------------------|------------------|-----------------------|
| ZrO_2 | 2818 | 2521 | 516.35 |
| YSZ | 2782 | 2986 | 538.94 |
| LaYSZ | 2953 | 3231 | 528.28 |
| NdYSZ | 2756 | 2947 | 566.18 |
| SmYSZ | 2691 | 2918 | 532.59 |

The melting points of the REYSZ materials were shown in Figure 9. The melting points of the REYSZ materials were 2521~3231 K, indicating that the materials could withstand working at higher temperatures and satisfied the requirement of high melting points of thermal barrier-coated ceramics, among which LaYSZ had the highest melting point. It was well-known that the Debye temperature of a material was closely related to the chemical bonding characteristics within the crystal; the stronger the chemical bonding, the higher the Debye temperature. According to the Debye theory, the characteristic Debye temperature originates from the thermal vibration of solid atoms and corresponds to the highest natural mode of oscillation of the crystal. As shown in Figure 9, it could be seen that the highest Debye temperature of NdYSZ was 566 K, indicating that the interatomic bonding of NdYSZ was the strongest among REYSZ.

Coatings 2024, 14, 1513 13 of 21

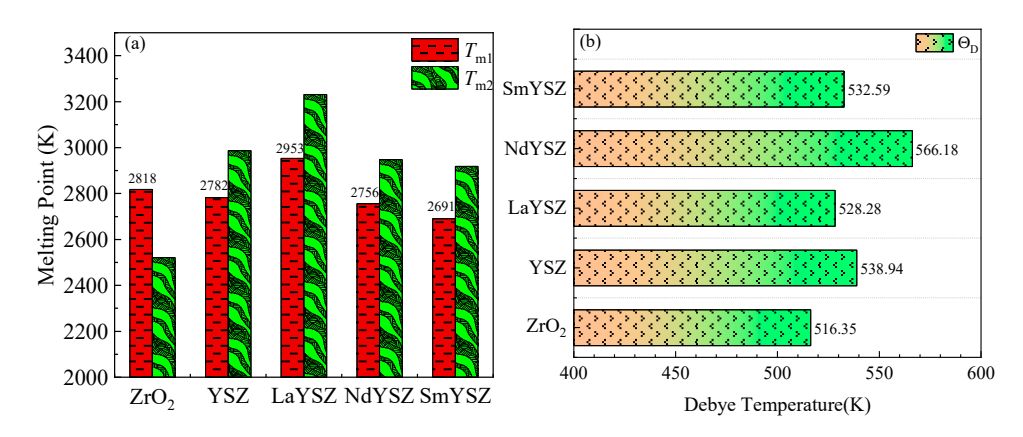


Figure 9. (a) Melting point of REYSZ material and (b) Debye temperature of REYSZ material.

3.2.5. Analysis of Phonon Rate and Minimum Thermal Conductivity

As shown in Table 6, the k_{min} values obtained by both the Cahill and Clarke models were relatively close to each other, indicating that it was feasible to predict the minimum thermal conductivity of REYSZ using the above model. The calculation results of the Clarke model were slightly lower than those of the Cahill model, which was because the Cahill model introduces the narrow range of freedom of phonons in the amorphous state to measure the thermal conductivity of the material. As shown in Figure 10, the lowest thermal conductivity of the REYSZ material was 2.355~2.715 W/m·K, and the thermal conductivity of the NdYSZ material was very close to that of YSZ. The reason for this was, firstly, the structure of REYSZ was more complex, and there were many tilted Zr-O and RE-O polyhedral structures in the crystal structure of REYSZ in the tetragonal phase, and these highly complex structures reduced the symmetry within the system. As the ionic radius of the lanthanide rare earth elements decreases, the tilt of the RE-O polyhedron further increases, and the degree of distortion within the crystal lattice increases. Finally, the large differences in ionic radii, atomic masses, and charges led to the diversification of chemical bonding species and bond lengths in REYSZ and the intensification of phonon scattering, which ultimately produced low intrinsic thermal conductivity, and the low thermal conductivity values of REYSZ were favorable for its move towards practical applications.

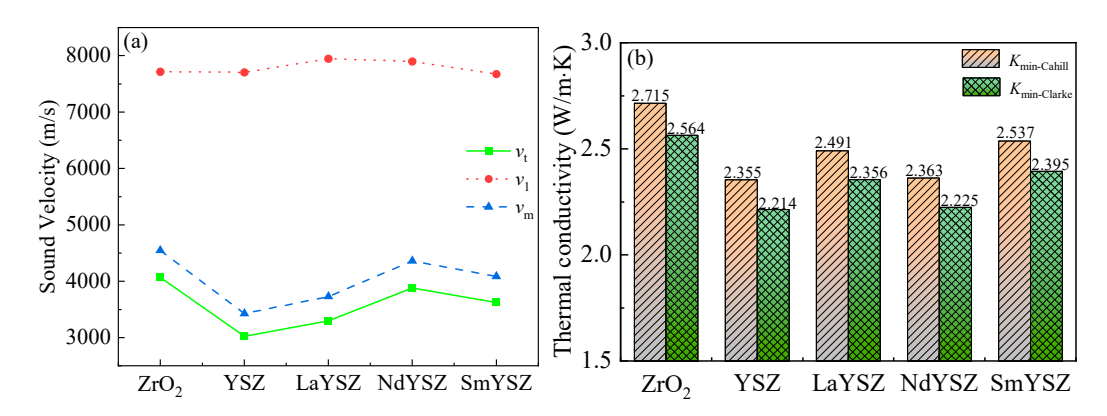


Figure 10. (a) Phonon rate of REYSZ material and (b) minimum thermal conductivity of REYSZ material.

Coatings 2024, 14, 1513 14 of 21

| Crystal | V_{t} | V_1 | $V_{\mathbf{M}}$ | K _{min-Cahill} | K _{min-Clarke} |
|---------|---------|---------|------------------|-------------------------|-------------------------|
| ZrO_2 | 4069.35 | 7714.17 | 4547.56 | 2.715 | 2.564 |
| YSZ | 3023.39 | 7706.27 | 3426.17 | 2.355 | 2.214 |
| LaYSZ | 3296.97 | 7948.17 | 3730.67 | 2.491 | 2.356 |
| NdYSZ | 3883.29 | 7900.25 | 4359.84 | 2.363 | 2.225 |
| SmYSZ | 3625.28 | 7675.48 | 4085.39 | 2.537 | 2.395 |

Table 6. Phonon rate (m/s) and minimum thermal conductivity $(W/m \cdot K)$ of REYSZ ceramic materials.

3.2.6. Analysis of the Coefficient of Thermal Expansion

Under a high-temperature service environment, due to the mismatch of the coefficient of thermal expansion between the ceramic coating and the metal bonding layer, a large thermal mismatch stress would be generated at the interface, which contributed to the sprouting and expansion of cracks during thermal cycling, leading to the cracking and detachment of the ceramic coating in the direction parallel or perpendicular to the metal substrate, which seriously affected its service life. As shown in Figure 11, the thermal expansion coefficients of REYSZ materials were $6.773\sim7.432\times10^{-6}~{\rm K}^{-1}$, in which both NdYSZ and SmYSZ have a better performance compared with the traditional YSZ, which was expected to be a new type of post-selected material for thermal barrier coatings. Although the doping of rare earth elements could improve the thermal expansion coefficient of thermal barrier coatings, it might also deteriorate other properties, so the effects of the valence, ionic radius, and content of the elements on the lattice of YSZ needed to be considered comprehensively. Calculations with the help of first nature principle modeling were an effective means of obtaining a suitable doping system, which was also one of the hot spots in the current research on the modification of YSZ material.

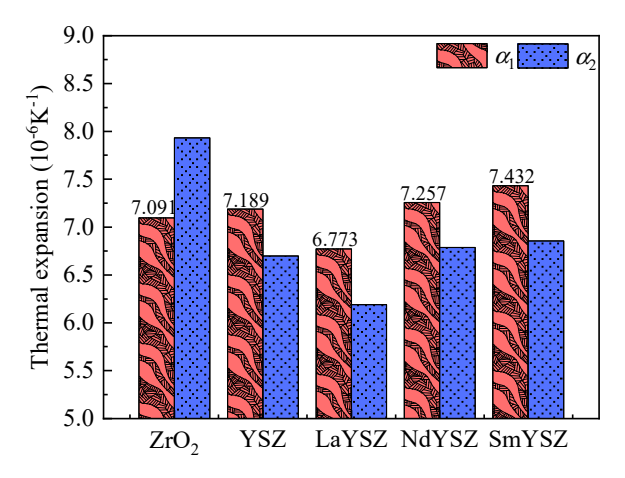


Figure 11. Coefficient of thermal expansion of REYSZ material.

3.3. Analysis of Corrosion Resistance to CMAS

The data used in the model surface energy calculation process and the results of the calculations were shown in Table 7. Through the surface energy calculation, the stable surface structures with the lowest energy (YSZ-II, LaYSZ-I, SmYSZ- II, and NdYSZ-IV) were selected as the base model for constructing the interfacial model, and the interfacial model was obtained by constructing it together with the amorphous CMAS cells, as shown in Figure 2.

Coatings 2024, 14, 1513 15 of 21

Table 7. Surface energy of surface models.

| Crystal | | E _{slab} /eV | E _{bulk} /eV | $E_{surface}/(J/m^2)$ |
|---------------|-----------|-----------------------|-----------------------|-----------------------|
| | YSZ-I | -66,119.37796 | -33,078.98941 | 3.49696 |
| VC7 (1 1 1) | YSZ-II | -66,121.17506 | -33,078.98941 | 3.33415 |
| YSZ (1 1 1) | YSZ-III | -66,112.40976 | -33,078.98941 | 4.12823 |
| | YSZ-IV | $-66,\!119.37934$ | -33,078.98941 | 3.49683 |
| | LaYSZ-I | -65,718.37322 | -32,890.35333 | 5.64697 |
| LaVC7 (1.1.1) | LaYSZ-II | -65,711.08193 | -32,890.35333 | 6.30751 |
| LaYSZ (1 1 1) | LaYSZ-III | -65,715.16314 | -32,890.35333 | 5.93778 |
| | LaYSZ-IV | -65,711.08245 | -32,890.35333 | 6.30746 |
| | SmYSZ-I | -71,461.37647 | -35,754.78252 | 4.36554 |
| SmYSZ (1 1 1) | SmYSZ-II | -71,464.32894 | -35,754.78252 | 4.09807 |
| 311113Z (111) | SmYSZ-III | -71,459.40144 | -35,754.78252 | 4.54447 |
| | SmYSZ-IV | -71,457.82904 | -35,754.78252 | 4.68691 |
| | NdYSZ-I | -68,792.47303 | -34,415.54697 | 3.49878 |
| NAVC7 (1 1 1) | NdYSZ-II | -68,796.27802 | -34,415.54697 | 3.15408 |
| NdYSZ (1 1 1) | NdYSZ-III | -68,792.46137 | -34,415.54697 | 3.49984 |
| | NdYSZ-IV | -68,796.54301 | -34,415.54697 | 3.13007 |

The Griffith fracture energy of the three models could be calculated from the fracture energy Formula (2), and the simulation data involved were shown in Table 8. From the calculation results, it could be seen that the Griffith fracture energy of the CMAS/NdYSZ system $(6.934 \, \text{J/m}^2)$ was much smaller than that of the CMAS/YSZ system $(8.218 \, \text{J/m}^2)$. The surface energy of the material was also an important factor affecting its anti-wetting property, and a lower surface energy was undoubtedly beneficial in increasing the wetting angle between the molten CMAS and the coating surface, which affected the melt penetration behavior. Comparing the surface energies of the four modeled surface structures, it could be seen (shown in Table 7) that the NdYSZ model had the lowest surface energy $(3.130 \, \text{J/m}^2)$ compared to the YSZ model $(3.334 \, \text{J/m}^2)$, the LaYSZ model $(5.646 \, \text{J/m}^2)$, and the SmYSZ model $(4.098 \, \text{J/m}^2)$.

Table 8. Interface model Griffith fracture energy.

| Crystal | E_{total}/eV | E_{CMAS}/eV | E_{REYSZ}/eV | $A/\rm{\AA}^2$ | $W/(J/m^2)$ |
|------------|-------------------------|------------------------|-------------------------|----------------|-------------|
| CMAS/YSZ | -93,468.1887 | -27,293.5967 | -66,121.1751 | 65.4679 | 8.218 |
| CMAS/LaYSZ | -93,072.9243 | -27,293.5967 | -65,718.3732 | 64.3453 | 9.473 |
| CMAS/SmYSZ | -98,814.6259 | -27,293.5967 | -71,464.3289 | 65.6354 | 8.638 |
| CMAS/NdYSZ | -96,134.7574 | -27,293.5967 | -68,796.5430 | 64.3458 | 6.934 |

3.4. Machine Learning Regression Prediction

Prediction of CMAS corrosion resistance of thermal barrier coatings by machine learning was implemented using BP neural network and ELM regression prediction models. A three-step process was carried out using dataset construction, model design and training, performance testing, and result evaluation. Firstly, based on the index analysis of the collected data in the first nature principle model building, the data set was constructed with the doping type and proportion as the inputs and the surface energy and fracture energy as the outputs, and the data were divided into a training set and test set for backup; then, the model was trained using the data from the training set, and the parameters were optimally adjusted according to the training results in order to achieve the best fitting effect, and finally, the prediction model was tested using the data from the test set. Finally, in order to objectively assess and validate the performance of the model, a five-fold cross-validation method was used. Cross-validation was a commonly used method to assess the performance of a model, which could reduce the dependence on the division of a single training and test set and improve the stability and reliability of the model. In this work,

five-fold cross-validation was used to assess the consistency and generalization ability of the model. Model feature importance analysis was used to explore the interrelationships between data within the model. Among the collected data, 100 sets of datasets were randomly divided into a 70% training set and 30% test set for model training and testing, respectively, and the applicability analysis of the established model was carried out to assess the actual prediction effect according to the prediction model in the prediction of corrosion performance against CMAS. As shown in Figure 12, this was a scatter plot of the fitting results of the BP neural network.

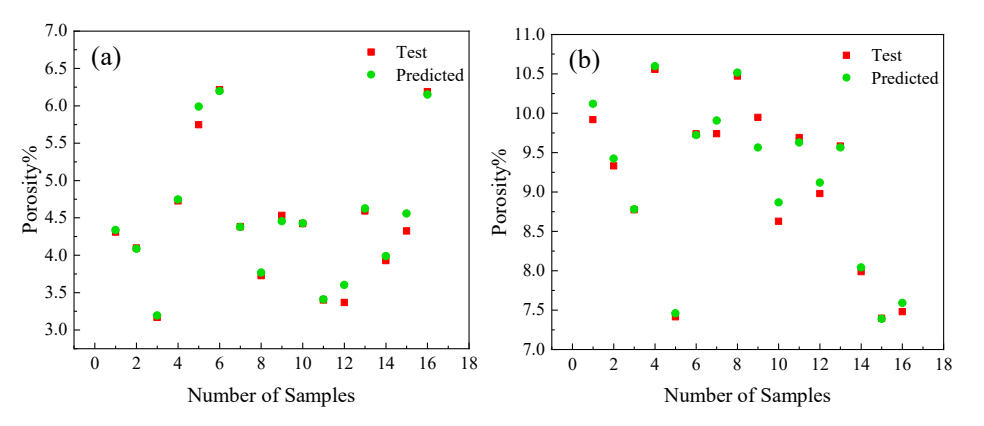


Figure 12. Scatterplot of fitting results for BP neural network output 1 (a) and output 2 (b).

As shown in Figure 13, it was a scatter plot of the fitting results of the extreme learning machine. To quantify the accuracy of the prediction models of the two samples, the mean square error, root mean square error, mean absolute error, and correlation coefficient were further used as the evaluation indexes to comprehensively and quantitatively evaluate the goodness-of-fit of the prediction models for the prediction of the training set of data and the generalization performance for the prediction of the extended set of data. The mean square error was the mean of the sum of the squares of the errors of the predicted values and the true value y. The mean absolute error was the absolute value of the difference with y. The correlation coefficient reflects the linear correlation with y.

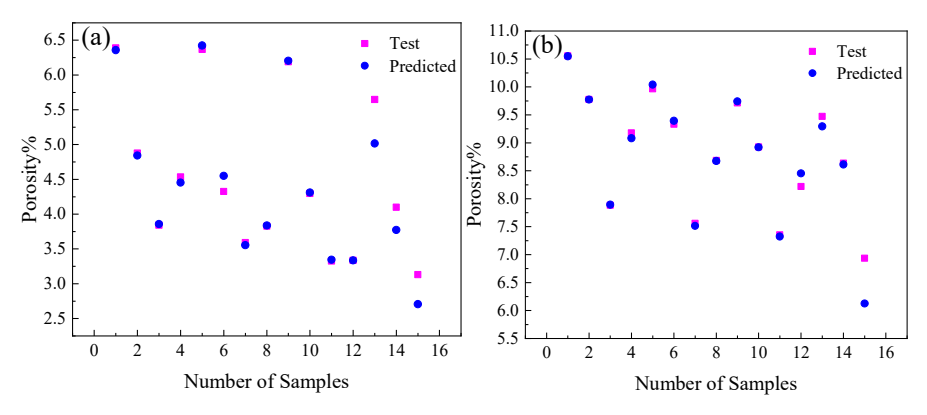


Figure 13. Scatterplot of fitting results for output 1 (a) and output 2 (b) of ELM.

After five-fold cross-validation, the accuracy and robustness of the prediction models need to be evaluated. To further validate the prediction accuracy of the two models, the performance of the different models was evaluated using error metrics and regression coefficients. By comparing the two error evaluation indexes, mean absolute error (MAE), and mean square error (MSE) and combining the regression coefficients of each model, the model prediction accuracy was further judged. As shown in Table 9, the MAE, MSE, and regression coefficients of output 1 of the BP neural network-based model were 0.1074, 0.0581, and 0.9579, respectively, and those of output 2 were 0.0846, 0.0659, and 0.9627,

respectively. The MAE, MSE, and regression coefficients of output 1 of the ELM model were 0.1278, 0.0946, and 0.9757, and the MAE, MSE, and regression coefficients for output 2 were 0.0932, 0.0935 and 0.9740, respectively.

Table 9. Evaluation of the accuracy of the prediction results of the anti-CMAS performance prediction model.

| K-Fold | Arithmetic | Output | MAE | MSE | R ² |
|---------------|------------|----------------|--------|--------|----------------|
| | DD | surface energy | 0.1147 | 0.082 | 0.9827 |
| K1 | BP | rupture energy | 0.0908 | 0.0706 | 0.9837 |
| KI | ELM | surface energy | 0.1425 | 0.0474 | 0.9647 |
| | ELIVI | rupture energy | 0.1079 | 0.0543 | 0.9506 |
| | BP | surface energy | 0.1873 | 0.0267 | 0.9232 |
| K2 | Dľ | rupture energy | 0.1352 | 0.1298 | 0.9413 |
| KZ | ELM | surface energy | 0.1253 | 0.1737 | 0.9636 |
| | ELIVI | rupture energy | 0.2372 | 0.2566 | 0.9714 |
| | DD. | surface energy | 0.1152 | 0.1095 | 0.9528 |
| 1/2 | BP | rupture energy | 0.0751 | 0.0687 | 0.9508 |
| K3 | ELM | surface energy | 0.1452 | 0.1745 | 0.9826 |
| | | rupture energy | 0.0751 | 0.0887 | 0.9803 |
| | DD. | surface energy | 0.0429 | 0.0486 | 0.9671 |
| 77.4 | BP | rupture energy | 0.0146 | 0.0422 | 0.9644 |
| K4 | TIM | surface energy | 0.1479 | 0.0438 | 0.9978 |
| | ELM | rupture energy | 0.0176 | 0.0572 | 0.9942 |
| | DD. | surface energy | 0.0751 | 0.0237 | 0.9637 |
| T/E | BP | rupture energy | 0.0184 | 0.0182 | 0.9732 |
| K5 | TI M | surface energy | 0.0781 | 0.0338 | 0.9734 |
| | ELM | rupture energy | 0.0284 | 0.0157 | 0.9737 |
| | DD | surface energy | 0.1074 | 0.0581 | 0.9579 |
| avorago value | BP | rupture energy | 0.0846 | 0.0659 | 0.9627 |
| average value | TIM | surface energy | 0.1278 | 0.0946 | 0.9757 |
| | ELM | rupture energy | 0.0932 | 0.0935 | 0.9740 |

In summary, a more comprehensive, accurate, and reliable prediction model was obtained by counting and analyzing the number of iterations and prediction results for each fold. In the five-fold cross-validation, the ELM showed high accuracy and robustness, thus providing strong support for practical applications. Meanwhile, the analysis of the evaluation metrics also demonstrated the superiority of the machine learning regression prediction model in the prediction of CMAS corrosion resistance of thermal barrier coatings. The results of these analyses would provide important references for further optimization of the model and prediction applications.

The core of this study was to combine first principles with machine learning to provide a relatively novel data-driven and mechanism-driven fusion of new material development methodology for model prediction of thermomechanical properties and CMAS corrosion resistance of thermal barrier coatings and further service the life assessment of thermal barrier coatings. A simple and efficient high-throughput screening method for thermal barrier coating materials was established by starting from a first-principles computational method and going down to the atomic level. This method could effectively predict the CMAS corrosion resistance and other thermal and mechanical properties of material for thermal barrier coatings. According to the development strategy of a new CMAS corrosion-resistant material for thermal barrier coatings proposed in the article, a new thermal barrier coatings material was designed and comprehensively compared with the conventional YSZ material in terms of CMAS corrosion resistance, the thermal expansion coefficient, thermal conductivity, fracture toughness, and hardness. The results were shown in Figure 14. The results of the study further confirmed the accuracy and feasibility of using first-

Coatings 2024, 14, 1513 18 of 21

principle calculation methods for the design and development of the material for thermal barrier coatings.

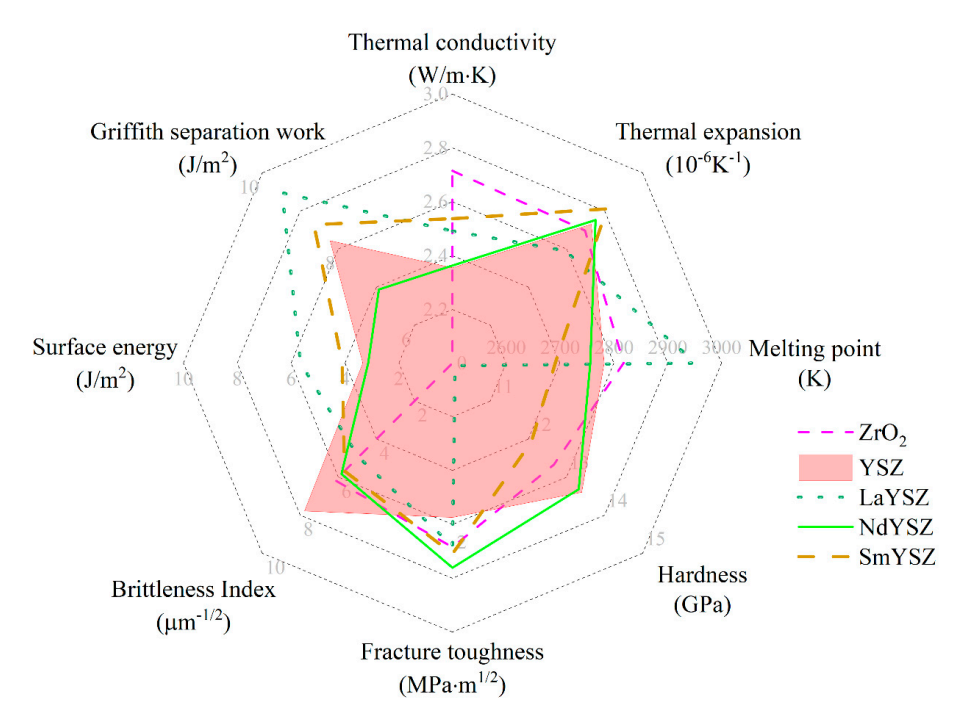


Figure 14. Radar diagram of the comprehensive performance distribution of REYSZ materials.

In the process of machine learning model construction, these feature parameters were fused as inputs and trained and optimized by the machine learning model, which was combined with the K-fold cross-validation method to improve the accuracy and stability of the prediction line. This demonstrated the great potential for the application of machine learning in materials research, broadened the scope of machine learning in materials science, and provided a new avenue for the development of new materials for thermal barrier coatings.

In conclusion, this study not only provided insights into the issues of model selection as well as prediction accuracy but also highlighted the innovative application of first principles and machine learning in the prediction of the CMAS corrosion resistance of thermal barrier coatings. This application was expected to provide a new scientific research paradigm in the field of materials science and engineering, offering a more viable and effective approach to materials development for thermal barrier coatings.

4. Conclusions

In this work, a more systematic theoretical prediction and evaluation of the crystal structure, elastic properties, thermal–mechanical properties, and CMAS corrosion resistance of REYSZ (RE = La, Sm, Nd) materials was carried out using a first-principles approach based on density functional theory. The calculated metrics included energy stability, mechanical stability, the modulus of elasticity, Poisson's ratio, Pugh's ratio, hardness, fracture toughness, the critical energy release rate, the melting point, Debye's temperature, the phonon rate, thermal conductivity, the coefficient of thermal expansion, surface energy, Griffith's fracture energy, and regression prediction of the new material's resistance to CMAS corrosion using a machine learning model. The following conclusions were obtained.

(1) The formation process of the tetragonal phase REYSZ was exothermic and thermodynamically stable, satisfying the mechanical stability criterion. The enthalpies of the formation of REYSZ were all negative, indicating that the formation of the compound system was an exothermic process; i.e., the material was thermodynamically stable in the ground state. Near the Fermi energy level, none of the electronic state densities Coatings **2024**, 14, 1513 19 of 21

were zero, indicating that all REYSZ phases exhibit metallic properties. The N(EF) values of the two phases YSZ and LaYSZ were close to each other, with the p-orbitals providing the energy near the Fermi energy level, and the doped rare earth elements Y and La contributing less at the Fermi energy level. The N(EF) values of the two phases NdYSZ and SmYSZ were closer together than the first two, and the structural stability was reduced. The difference lies in the provision of energy near the Fermi energy level by f orbitals, which were not present in the former two, and in the larger contribution to the total density of states by the rare earth elements Nd and Sm. Its Young's modulus and bulk modulus were large, and its shear modulus was small (49.52–91.10 GPa), indicating that the REYSZ material was susceptible to deformation by shear stress. The hardness of REYSZ material was 10.069~13.398 GPa, the fracture toughness was $1.722 \sim 2.283 \text{ MPa-m}^{1/2}$, and the brittleness index was $4.938 \sim 7.780 \, \mu \text{m}^{-1/2}$, which indicated that the mechanical properties of the REYSZ material were excellent, with a large strain-damage tolerance, and it was not easy to break under the effect of applied loads and thermal shocks. The melting point of REYSZ was 2691~2818 K, the Debye temperature was 516.35~566.18 K, and the lowest thermal conductivity was 2.355~2.715 W/m·K (Cahill model) and 2.214~2.564 W/m·K (Clarke). This low thermal conductivity created a large temperature gradient between the alloy substrate and the high-temperature gas, which protected metal parts from heat damage and improved the efficiency of turbine engines. In addition, the coefficients of thermal expansion of 6.773~7.432 \times 10⁻⁶ K⁻¹ were all more favorable for the performance of REYSZ compared with the conventional YSZ system. Among them, the overall evaluation of the NdYSZ material was better.

- (2) The application of thermal barrier coatings was limited by CMAS erosion. In this work, the surface energy of the model and the Griffith fracture energy of the interfacial model were calculated, in which the NdYSZ model had the lowest surface energy $(3.130 \, \text{J/m}^2)$, and the CMAS/NdYSZ system had the lowest Griffith fracture energy $(6.934 \, \text{J/m}^2)$. Therefore, a comprehensive analysis showed that the rare earth element Nd₂O₃ has the potential to improve the resistance of zirconia-based materials for thermal barrier coatings to CMAS corrosion. To reduce the variability with YSZ materials, and thus the degree of mismatch between the multilayers, co-doping zirconia materials using Nd₂O₃ and Y₂O₃ would perhaps provide better overall service performance.
- In this paper, quantitative parameters that characterize the CMAS resistance of materials, namely surface energy and fracture energy, were derived based on first-principle simulations. Detection of the CMAS corrosion resistance of thermal barrier coatings was performed by a data-driven predictive model. The inputs were the doping species and ratios, and the outputs were the surface and fracture energies. The processed 100 sets of data were divided into a training set and a validation set. Regression prediction of CMAS corrosion resistance after rare earth doping of YSZ combined with five-fold cross-validation was performed. From the simulation results, the prediction error of the extreme learning machine model was very small, the accuracy was significantly higher than that of the BP traditional model, and the coefficient of determination R² reached 0.975; the model regression effect was good. According to the simulation data, the CMAS resistance of the rare earth-doped coating was significantly improved compared to the conventional YSZ coating. It could be seen that the data-driven prediction model shows excellent performance in the CMAS corrosion resistance of thermal barrier coatings, and this study was conducive to enriching the methodological system for the assessment of the CMAS corrosion resistance of thermal barrier coatings.

Author Contributions: Conceptualization, D.Y., Y.W., and H.F.; Data curation, F.W.; Formal analysis, F.W. and C.Y.; Funding acquisition, D.Y. and H.F.; Investigation, F.W., Y.W., C.Y., and H.L.; Methodology, D.Y. and C.Y.; Project administration, D.Y., Z.X., Y.W., and H.L.; Resources, D.Y., Z.X., and

H.F.; Software, F.W., C.Y., and H.F.; Supervision, D.Y., Z.X., H.F., and H.L.; Validation, F.W., Y.W., and H.L.; Visualization, F.W.; Writing—original draft, F.W.; Writing—review and editing, D.Y. and H.F. All authors have read and agreed to the published version of the manuscript.

Funding: This research was funded by the National Natural Science Foundation of China (No. 52205547, D.Y., No. 52305169, H.F.), the Excellent Young Talents Fund of Higher Education Institutions of Anhui Province (No. 2024AH030006, D.Y.), the Key Research and Development Projects in Anhui Province (2022a05020004, D.Y.), Industry–University Research Project (No. HX-2024-04-054, D.Y., No. HX-2024-09-085, D.Y.), the Undergraduate Teaching Quality Improvement Program Project of Anhui Polytechnic University (No. 2023jyxm76, D.Y., No. 2023szyzk39, D.Y., 2024szyzk51).

Institutional Review Board Statement: Not applicable.

Informed Consent Statement: Not applicable.

Data Availability Statement: Data are contained within the article.

Conflicts of Interest: The authors declare no conflicts of interest.

References

1. Zhang, X.; Deng, Z.; Li, H.; Mao, J.; Deng, C.; Deng, C.; Niu, S.; Chen, W.; Song, J.; Fan, J.; et al. Al₂O₃-modified PS-PVD 7YSZ thermal barrier coatings for advanced gas-turbine engines. *Npj Mat. Degrad.* **2020**, *4*, 31. [CrossRef]

- 2. Leckie, R.M.; Krämer, S.; Rühle, M.; Levi, C.G. Thermochemical compatibility between alumina and ZrO₂-GdO_{3/2} thermal barrier coatings. *Acta Mater.* **2005**, *53*, 3281–3292. [CrossRef]
- 3. Yang, Z.; Wang, W.; Deng, S.; Fang, H.; Yang, T.; Wang, L. Thermal shock behavior and particle erosion resistance of toughened GZ coatings prepared by atmospheric plasma spraying. *Coatings* **2021**, *11*, 1477. [CrossRef]
- 4. Evans, A.G.; Mumm, D.R.; Hutchinson, J.W.; Meier, G.H.; Pettit, F.S. Mechanisms controlling the durability of thermal barrier coatings. *Prog. Mater. Sci.* **2001**, *46*, 505–553. [CrossRef]
- 5. Clarke, D.R.; Oechsner, M.; Padture, N.P. Thermal-barrier coatings for more efficient gas turbine engines. *MRS Bull.* **2012**, 37, 891–898. [CrossRef]
- 6. Levi, C.G.; Hutchinson, J.W.; Vidal-S'etif, M.; Johnson, C.A. Environmental degradation of thermal barrier coatings by molten deposits. *MRS Bull.* **2012**, *37*, 932–941. [CrossRef]
- 7. Shan, X.; Zou, Z.; Gu, L.; Yang, L.; Guo, F.; Zhao, X.; Xiao, P. Buckling failure in air-plasma sprayed thermal barrier coatings induced by molten silicate attack. *Scr. Mater.* **2016**, *113*, 71–74. [CrossRef]
- 8. Song, W.; Lavallée, Y.; Hess, K.-U.; Kueppers, U.; Cimarelli, C.; Dingwell, D.B. Volcanic ash melting under conditions relevant to ash turbine interactions. *Nat. Commun.* **2016**, *7*, 10795. [CrossRef] [PubMed]
- 9. Cai, Z.; Jiang, J.; Wang, W.; Liu, Y.; Cao, Z. CMAS penetration-induced cracking behavior in the ceramic top coat of APS TBCs, Ceram. *Int.* **2019**, *45*, 14366–14375.
- 10. Jackson, R.W.; Begley, M.R. Critical cooling rates to avoid transient-driven cracking in thermal barrier coating (TBC) systems. *Int. J. Solids Struct.* **2014**, *51*, 1364–1374. [CrossRef]
- 11. Krämer, S.; Yang, J.; Levi, C.G.; Johnson, C.A. Thermochemical interaction of thermal barrier coatings with molten CaO-MgO-Al₂O₃-SiO₂ (CMAS) deposits. *J. Am. Ceram. Soc.* **2006**, *89*, 3167–3175. [CrossRef]
- 12. Li, L.; Hitchman, N.; Knapp, J. Failure of thermal barrier coatings subjected to CMAS attack. *J. Therm. Spray. Technol.* **2010**, 19, 148–155. [CrossRef]
- 13. Guo, L.; Yan, Z.; Yu, Y.; Yang, J.; Li, M. CMAS resistance characteristics of LaPO₄/YSZ thermal barrier coatings at 1250 °C–1350 °C. *Corros. Sci* **2019**, *154*, 111–122. [CrossRef]
- 14. Guo, L.; Li, M.; Cheng, Y.; Zhang, C.; He, S.; Zhang, Y.; Ye, F. Plasma sprayed nanostructured GdPO₄ thermal barrier coatings: Preparation microstructure and CMAS corrosion resistance. *J. Am. Ceram. Soc.* **2017**, *100*, 4209–4218. [CrossRef]
- 15. Rahaman, M.N.; Gross, J.R.; Dutton, R.E.; Wang, H. Phase stability, sintering, and thermal conductivity of plasma-sprayed ZrO₂-Gd₂O₃ compositions for potential thermal barrier coating applications. *Acta Mater.* **2006**, *54*, 1615–1621. [CrossRef]
- Song, D.; Song, T.; Paik, U.; Lyu, G.; Kim, J.; Yang, S.; Jung, Y.G. Hot-corrosion resistance and phase stability of Yb₂O₃-Gd₂O₃-Y₂O₃ costabilized zirconia-based thermal barrier coatings against Na₂SO₄+V₂O₅ molten salts. Surf. Coat. Tech. 2020, 400, 126197. [CrossRef]
- 17. Gul, S.R.; Khan, M.; Zeng, Y.; Wu, B. Theoretical investigations of electronic and thermodynamic properties of Ce doped La₂Zr₂O₇ pyrochlore. *Mater. Res. Express* **2019**, *6*, 085210. [CrossRef]
- 18. Yin, J.; Lu, X. Theoretical study of electronic structure and optical properties of tin doped CuS counter electrode for dyesensitized solar cells. *Sol. Energy* **2018**, *171*, 871–875. [CrossRef]
- 19. Khan, A.; Song, P.; Huang, T.; Zhou, Y.; Xiong, X.; Li, C.; Lü, J.; Chen, R.; Lu, J. Diffusion characteristics and structural stability of Pt modified β-NiAl/γ'-Ni₃Al within NiCoCrAl alloy at high temperature. *Appl. Surf. Sci.* **2019**, *476*, 1096–1107. [CrossRef]
- 20. Yu, J.; Lin, X.; Wang, J.; Chen, J.; Huang, W. First-principles study of the relaxation and energy of bccFe, fcc-Fe and AISI-304 stainless steel surfaces. *Appl. Surf. Sci.* **2009**, 255, 9032–9039. [CrossRef]

21. Li, B.; Chen, Z.; Zheng, H.; Li, G.; Li, H.; Peng, P. Wetting mechanism of CMAS melt on YSZ surface at high temperature: First-principles calculation. *Appl. Surf. Sci.* **2019**, *483*, 811–818. [CrossRef]

- 22. Adam, N.K. Use of the term 'Young's equation' for contact angles. Nature 1957, 180, 809-810. [CrossRef]
- 23. Mazhnik, E.; Oganov, A.R. A model of hardness and fracture toughness of solids. J. Appl. Phys. 2019, 126, 125109. [CrossRef]
- 24. Liu, Z.; Yuan, J.; Shen, J.; Hu, Y.; Chen, S. A new DEM calibration method for wet and stick materials based on the BP neural network. *Powder Technol.* **2024**, 448, 120228. [CrossRef]
- 25. Huang, G.; Wang, D.; Lan, Y. Extreme learning machines: A survey. Int. J. Mach. Learn. Cybern. 2011, 2, 107–122. [CrossRef]
- 26. Huang, G.B.; Zhu, Q.Y.; Siew, C.K. Extreme learning machine: Theory and applications. *Neurocomputing* **2006**, *70*, 489–501. [CrossRef]
- 27. Donhauser, J.; Doménech-Pascual, A.; Han, X.; Jordaan, K.; Ramond, J.-B.; Frossard, A.; Romaní, A.M.; Priemé, A. Modelling soil prokaryotic traits across environments with the trait sequence database ampliconTraits and the R package MicEnvMod. *Ecol. Inform.* 2024, 83, 102817. [CrossRef]
- 28. Bahri, E.A.; Zahraouy, E.H. Enhancing hydrogen storage properties of titanium hydride TiH2 with vacancy defects and uniaxial strain: A first-principles study. *Int. J. Hydrogen Energy* **2024**, *87*, *678*–685. [CrossRef]

Disclaimer/Publisher's Note: The statements, opinions and data contained in all publications are solely those of the individual author(s) and contributor(s) and not of MDPI and/or the editor(s). MDPI and/or the editor(s) disclaim responsibility for any injury to people or property resulting from any ideas, methods, instructions or products referred to in the content.